A Journal of the Gesellschaft Deutscher Chemiker
Angewandte Chemie
GDCh
International Edition
www.angewandte.org

Accepted Article

Title: Defect-Triggered Orbital Hybridization in FeMn Dual-Atom Catalysts Toward Sabatier-Optimized Oxygen Reduction

Authors: Mengxin Liu, Ying Li, Liu Yang, Pengcheng Zhao, Jingshuai Li, Lingtong Tian, Dapeng Cao, and Zhongwei Chen

To be cited as: *Angew. Chem. Int. Ed.* **2025**, e202505268

Link to VoR: https://doi.org/10.1002/anie.202505268

WILEY-VCH

RESEARCH ARTICLE

Defect-Triggered Orbital Hybridization in FeMn Dual-Atom Catalysts Toward Sabatier-Optimized Oxygen Reduction

Mengxin Liu[a, b]+, Ying Li[b]+, Liu Yang[b]*, Pengcheng Zhao[b], Jingshuai Li[b], Lingtong Tian[a], Dapeng Cao[a]*, Zhongwei Chen[b]*

[a] M. Liu, L. Tian, Prof. D. Cao
State Key Laboratory of Organic-Inorganic Composites, Beijing University of Chemical Technology, Beijing, 100029 China.
E-mail: caodp@mail.buct.edu.cn

[b] M. Liu, Y. Li, P. Zhao, J. Li, L.Yang, Prof. Z. Chen
State Key Laboratory of Catalysis, Power Battery & Systems Research Center, Dalian Institute of Chemical Physics, Chinese Academy of Sciences, Dalian, 110623, China.
E-mail: zwchen@dicp.ac.cn; liuyang93@dicp.ac.cn

[+] These authors contributed equally to this work.

Supporting information for this article is given via a link at the end of the document.

10.1002/anie.202505268

Abstract: Dual single-atom catalysts (DSAs), leveraging synergistic dual-site interactions, represent a promising frontier in electrocatalysis. However, the precise synthesis of dual-atom pairs and fine-tuning of their electronic structures remain significant challenges. Herein, we construct a defect-engineered heteronuclear FeMn-DSA anchored on a porous nitrogen-doped carbon matrix ($FeMn_{DSA}/d$NC) through a customized trinuclear-defect trapping strategy. This defect modulation strategy effectively stabilizes dual atomic pairs while optimizing electronic structures to approach Sabatier's optimality, significantly boosting oxygen reduction reaction (ORR) performance. The $FeMn_{DSA}/d$NC achieves a high half-wave potential of 0.921 V in alkaline media, with assembled zinc-air batteries demonstrating 291 mW cm^{-2} peak power density and stable charge/discharge cycling for over 500 h. Theoretical calculations reveal that defect-mediated coordination adjacent to Fe-Mn diatomic centers triggers charge redistribution, suppressing antibonding orbital populations while strengthening Fe $3d_{z^2}$ with O 2p orbital hybridization. This modulation weakens O-O bonding through optimized *OOH adsorption configurations, thereby enhancing ORR kinetics. The present work provides valuable insights into the precise modulation and the underlying mechanisms of DSAs, advancing the design of electrocatalysts for energy storage and conversion applications.

Introduction

Amidst escalating global energy crises and the imperative drive toward carbon neutrality, transformative advances in sustainable energy storage and conversion systems have become indispensable.[1] Central to these technologies, the oxygen reduction reaction (ORR) governs the efficiency of metal-air batteries and fuel cells through its multistep proton-coupled electron transfer pathways, yet suffers from inherently sluggish kinetics that constrain practical implementation.[2] Currently, platinum-based materials remain the benchmark for ORR, their widespread adoption is fundamentally limited by prohibitive costs and finite reserves.[3] Therefore, the development of earth-abundant electrocatalysts that combine exceptional activity, long-term stability, and economic viability to propel next-generation energy technologies.

Single-atom catalysts (SACs), renowned for their maximal atomic utilization and well-defined active-site architectures, have garnered significant attention in heterogeneous catalysis.[4] Among these, Fe SAC stands out as particularly notable for ORR, yet its typical $Fe-N_4$ coordination governed by D_{4h} symmetry, which constrain adsorption/desorption dynamics for critical intermediates like *OH.[5] Rational incorporation of a secondary heterometal to construct dual-single-atom catalysts (DSAs) emerges as a strategic solution, where asymmetric dual-site coordination disrupts local symmetry while synergistically redistributing electron density. This coordination engineering enables precise modulation of intermediate adsorption energetics, thereby enhancing ORR activity.[6] For instance, Fe adsorption on ZIF-8@ZIF-67 followed by pyrolysis yields FeCo-DSA, which features a high density of accessible active sites and demonstrates a half-wave potential of 0.889 V.[7] The Fe-Se DSA, synthesized via high-temperature treatment of Fe/ZIF-8 and Se powder, exhibits asymmetrical p-d orbital hybridization and superior bifunctional oxygen activity with a 0.698 V potential difference.[8] Despite advancements in DSAs, two persistent challenges impede their widespread adoption: (1) the lack of atomic-level precision in spatially arranging heteronuclear diatomic pairs, and (2) the inability to systematically approximate the Sabatier volcano apex through conventional bimetallic coordination strategies. While electronic modulation via heteroatom doping or strain engineering can enhance ORR activity, such approaches often fail to concurrently stabilize geometrically precise atomic configurations and thermodynamically optimize intermediate absorption energies. Defect engineering emerges as a transformative strategy to address these dual limitations. Structurally, vacancy defects (e.g., N vacancies, edge sites) act as topological anchoring points, strengthening metal-support interactions, thereby mitigating metal aggregation and enhancing structural robustness.[9] Electronically, these defects reconfigure the local coordination environment of dual-metal sites, enabling precise d-band center modulation and tailored oxygen absorption energetics. Therefore, the defect-driven approach holds significant potential for optimizing DSA catalyst performance, bringing it closer to the theoretical activity ceiling.

Drawing from prior insights, we strategically integrate defects into the FeMn-DSA system ($FeMn_{DSA}/d$NC) via a tailored trinuclear-defect trapping strategy, which stabilizes atomic pairs and precisely optimizes the electronic properties, driving the system toward its theoretical performance optimum. As anticipated, the $FeMn_{DSA}/d$NC catalyst demonstrates exceptional ORR performance with a half-wave potential ($E_{1/2}$) of 0.921 V, while zinc-air batteries utilizing it as the cathode achieve a power density of 291 mW cm^{-2} and maintain remarkable long-term stability, sustaining charge/discharge cycles at 5 mA cm^{-2} for over 500 h. Theoretical calculations reveal that defect incorporation near the FeMn diatomic site in $FeMn_{DSA}/d$NC triggers electron redistribution, promoting Fe $3d_{z^2}$ and O 2p orbital hybridization, which elongates the O-O bond and enhances *OOH adsorption, ultimately optimizing ORR kinetics.

Results and Discussion

The $FeMn_{DSA}/d$NC catalyst was synthesized through a precisely engineered trinuclear-defect trapping (TDT) strategy (Figure 1a), involving the co-encapsulation of a Fe_2Mn trinuclear cluster and melamine (MA) within ZIF-8 frameworks via a host-guest assembly. Pyrolysis of the resulting Fe_2Mn/MA@ZIF-8 precursor induces thermal decomposition of MA, generating ammonia that etches the carbon matrix to create a defect-rich architecture while simultaneously enriching nitrogen content.[10] This engineered defect environment stabilizes Fe/Mn species liberated from Zn evaporation and cluster ligand decomposition, ensuring their atomic dispersion through strong metal-support

10.1002/anie.202505268

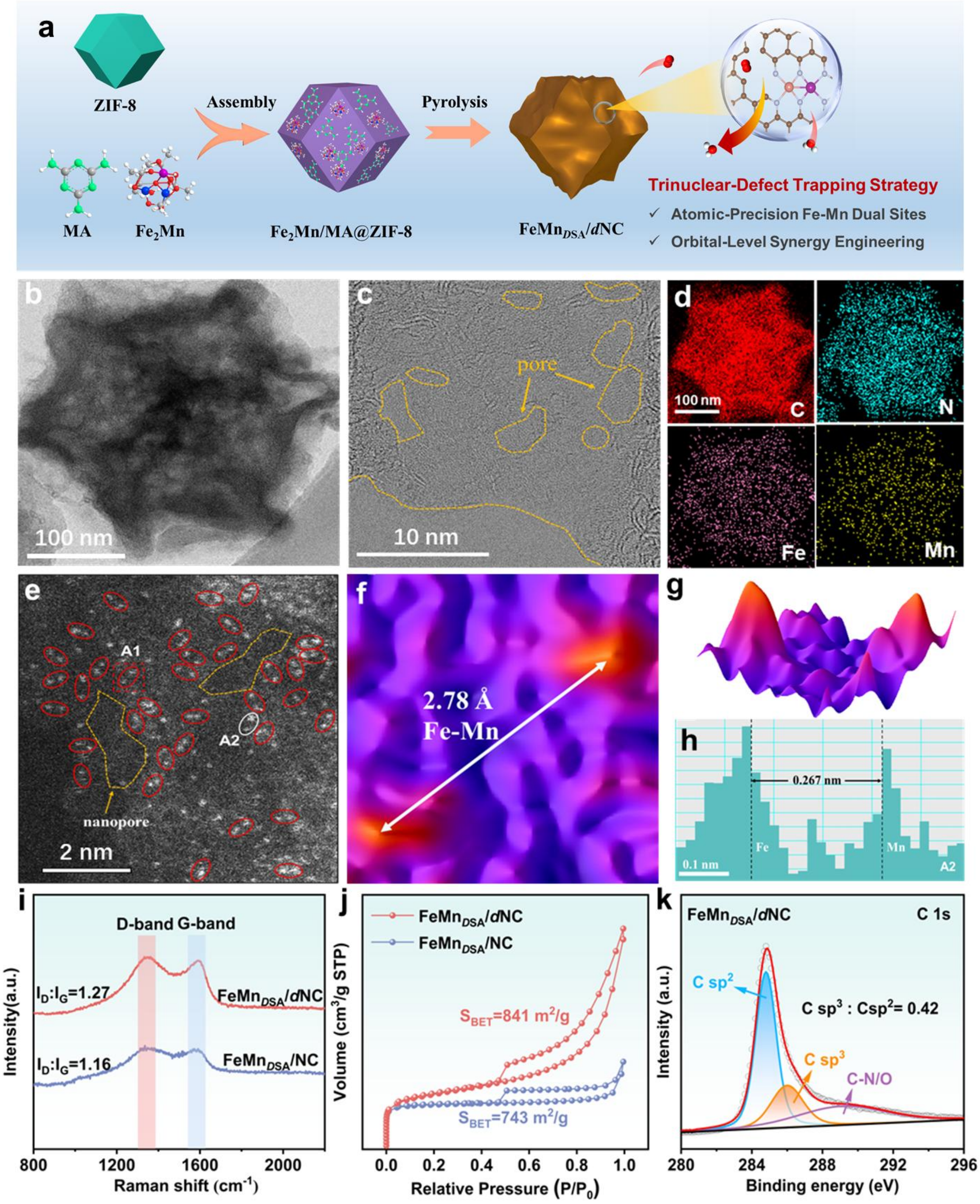

Figure 1. Synthesis and characterizations of FeMn$_{DSA}$/*d*NC. (a) Schematic illustration of the synthetic process for FeMn$_{DSA}$/*d*NC. (b) TEM, and (c) HRTEM images of FeMn$_{DSA}$/*d*NC. (d) Elemental mapping images of FeMn$_{DSA}$/*d*NC. (e) HAADF-STEM image of FeMn$_{DSA}$/*d*NC, showing the dual atom (red ellipse). (f) The intensity profiles and (g) 3D model in the A1 region. (h) The intensity profiles in the A2 region. (i) Raman spectra and (j) N_2 adsorption/desorption isotherms of FeMn$_{DSA}$/*d*NC and FeMn$_{DSA}$/NC. (k) C 1s XPS spectra for FeMn$_{DSA}$/*d*NC.

interactions. The process yields a defective carbon matrix with uniformly anchored FeMn dual-atom pairs (FeMn$_{DSA}$/*d*NC). Control samples of FeMn$_{DSA}$/NC (MA-free), Fe$_{SA}$/NC (Fe$_2$Zn-based), and *d*NC (Fe$_2$M-free) were synthesized analogously for comparative analysis (see Supporting Information). The trinuclear metal clusters, Fe$_2$M feature a highly coordinated structure where each Fe$^{III}_2$ and M atom is coordinated by six carboxylic acid ligands, with a μ$_3$-oxo bridge seamlessly connecting the three adjacent metal centers (Figure S1). The crystal structure and composition of Fe$_2$M were thoroughly characterized using X-ray diffraction (XRD), scanning electron microscopy (SEM), and Fourier transform infrared spectroscopy (FT-IR), with results consistent with previous literature (Figures S2–S4).[11] Further, XRD patterns of Fe$_2$Mn/MA@ZIF-8 align closely with those of pristine ZIF-8 (Figure S5), and SEM characterization collectively demonstrates that Fe$_2$Mn/MA incorporation preserves both the crystallographic integrity and morphological features of the ZIF-8 framework (Figures S6 and S7).

Transmission electron microscopy (TEM) and SEM images of FeMn$_{DSA}$/*d*NC unveil a defect-rich, porous architecture with preserved rhombic dodecahedral morphology, devoid of metallic aggregates or oxides (Figure 1b,c and Figure S8a), ensuring maximal active-site exposure and enhanced mass transport kinetics. In contrast, FeMn$_{DSA}$/NC and Fe$_{SA}$/NC samples exhibit limited pore structures (Figures S8b,c and S9), highlighting the crucial role of MA in creating defects. XRD pattern of FeMn$_{DSA}$/*d*NC displays only two graphitic carbon peaks at ~25° and ~44° (Figure S10), with no detectable diffraction peaks for metal particles. Energy-dispersive X-ray spectroscopy (EDS) mapping reveals a homogeneous spatial distribution of C, N, Fe, and Mn elements throughout the structure (Figure 1d). Spherical aberration-corrected high-angle annular dark-field STEM (HAADF-STEM) directly visualizes Fe-Mn diatomic pairs (bright spots in Figure 1e) preferentially anchored at nanopore edges. Intensity profiles in Figure 1f and 1g (region A1) quantify an Fe-Mn interatomic distance of ~2.78 Å, while Figure 1h (region A2) reveals a 0.267 nm distance between Fe and Mn atoms, confirming successful construction of robustly coupled FeMn diatomic configurations. Inductively coupled plasma optical emission spectroscopy (ICP-OES) measurements confirm Fe and Mn loadings of 2.82 wt% and 1.16 wt%, respectively. Raman spectroscopy analysis of FeMn$_{DSA}$/*d*NC reveals two characteristic peaks (Figure 1i): the defect-related D band (1350 cm^{-1}) and the graphite-related G band (1590 cm^{-1}).[12] The calculated I$_D$/I$_G$ ratio of 1.27 for FeMn$_{DSA}$/*d*NC is higher than that of FeMn$_{DSA}$/NC (1.16), suggesting a greater degree of defects in FeMn$_{DSA}$/*d*NC. Moreover, nitrogen adsorption-desorption isotherms demonstrate that FeMn$_{DSA}$/*d*NC displays a typical Type IV isotherm, with the pore size distribution analysis revealing the presence of both micropores and mesopores (Figure 1j, Figure S11 and Table S1). The higher Brunauer-Emmett-Teller (BET) specific surface area of FeMn$_{DSA}$/*d*NC (841 m^2 g^{-1}) compared to FeMn$_{DSA}$/NC (743 m^2 g^{-1}) underscores MA's crucial role in defect engineering and pore structure optimization. This MA-derived defect engineering synergistically enhances atomic anchoring, reactant accessibility, and charge/mass transfer dynamics, as rationalized by the superior electrochemical performance of the catalyst.

The surface chemical composition and valence states of the synthesized samples were analyzed by X-ray photoelectron spectroscopy (XPS). The survey spectrum of FeMn$_{DSA}$/*d*NC confirms the coexisting peaks for C, N, Fe and Mn signatures (Figure S12), with attenuated metal signals reflecting their atomic-level dispersion. The high-resolution C 1s spectra of FeMn$_{DSA}$/*d*NC, FeMn$_{DSA}$/NC, and Fe$_{SA}$/NC (Figure 1k and Figure S13) can be deconvoluted into three components: sp^2-hybridized graphitic C=C (284.8 eV), sp^3-hybridized defective C-C (286.0 eV), and C-N/O (289.1 eV).[13] The elevated sp^3/sp^2 ratio of FeMn$_{DSA}$/*d*NC (0.42 vs. 0.37 for FeMn$_{DSA}$/NC) indicates its increased defect density, aligning with Raman spectroscopic trends. The high-resolution N 1s spectrum of FeMn$_{DSA}$/*d*NC

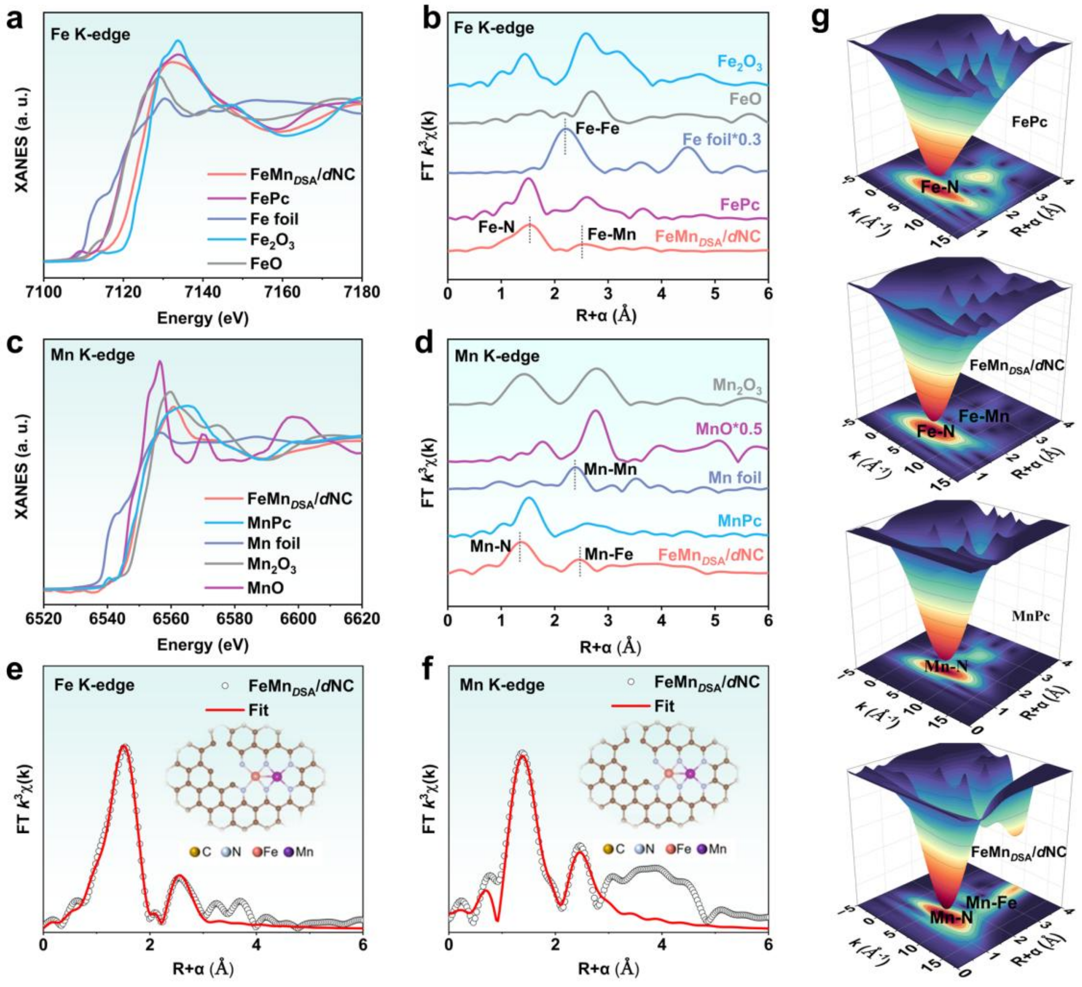

Figure 2. X-ray adsorption spectroscopy results for FeMn$_{DSA}$/*d*NC and reference samples. (a) Normalized Fe K-edge XANES spectra, and (b) Fourier transform of k^3-weighted EXAFS spectra. (c) The normalized Mn K-edge XANES spectra, and (d) Fourier transform of k^3-weighted EXAFS spectra. (e,f) FT-EXAFS fitting curve in *R* space of FeMn$_{DSA}$/*d*NC at the Fe and Mn K-edges, with the inset showing the corresponding schematic model. (g) WT plots of FeMn$_{DSA}$/*d*NC, FePc and MnPc samples.

(Figure S14) can be resolved to pyridine N (398.4 eV), metal-N (399.3 eV), pyrrole N (400.5 eV), graphitic N (401.4 eV), and oxidized N (403.2 eV), respectively.[14] Quantitative analysis reveals a higher Fe/Mn-N coordination ratio in FeMnDSA/dNC (17.1%) compared to FeMnDSA/NC (14.2%), directly confirming the increased density of catalytically active sites, which drives enhanced ORR activity. As depicted in Figures S15 and S16, the Fe 2p spectrum features peaks at 711.0 eV ($2p_{3/2}$) and 724.5 eV ($2p_{1/2}$), whereas the Mn 2p spectrum manifests peaks at 641.6 eV ($2p_{3/2}$) and 653.3 eV ($2p_{1/2}$).[15] $FeMn_{DSA}$/*d*NC exhibits a shift in Fe 2p and Mn 2p peaks towards higher and lower binding energies compared to $FeMn_{DSA}$/NC, indicative of electron redistribution between Fe and Mn due to defect engineering, which favors the regulation of intermediate adsorption/desorption during ORR.

To elucidate the electronic structure and local coordination environment of the $FeMn_{DSA}$/*d*NC catalyst, X-ray absorption near-edge structure (XANES) and extended X-ray absorption fine structure (EXAFS) spectroscopy were further conducted.[16] The Fe K-edge XANES spectrum (Figure 2a) reveals an absorption edge positioned between FeO and Fe_2O_3, indicating an oxidation state of Fe between +2 and +3. Fourier-transformed k^3-weighted EXAFS spectrum (Figure 2b) exhibits a primary Fe-N coordination shell at ~1.50 Å and a secondary Fe-Mn scattering path at ~2.45 Å, unambiguously confirming heteronuclear Fe-Mn coupling.[17] Similarly, the Mn K-edge XANES (Figure 2c) aligns with MnPc, signifying a predominant Mn^{2+} oxidation state, while EXAFS (Figure 2d) identifies Mn-N bonds at ~1.38 Å and replicates the Fe-Mn interatomic distance at ~2.45 Å, validating reciprocal metal-metal coordination. The least-squares EXAFS fitting (Figure 2e,f) deciphers the diatomic architecture: Fe atoms are coordinated with four nitrogen atoms and are bonded to one Mn atom, while Mn atoms exhibit analogous N_4 coordination and reciprocally couple to Fe via antipodal Mn-Fe bonds (Figure S17 and Table S2). Wavelet-Transform (WT) analysis was further employed to resolve atomic-scale coordination environments. As shown in Figure 2g and S18, the maximum intensity values for Fe and Mn in $FeMn_{DSA}$/*d*NC (4.8 $Å^{-1}$ and 5.1 $Å^{-1}$ in k-space) differ from those of Fe foil (8.2 $Å^{-1}$) and Mn foil (7.7 $Å^{-1}$), unambiguosly validating the absence of metal clustering and establishing heteronuclear Fe-Mn diatomic pairs. These comprehensive characterizations verify the defect-stabilized FeMn dual-site architecture within N-doped carbon matrix, achieved through the precisely engineered TDT synthetic protocol.

Electrocatalytic ORR performance of the synthesized catalysts was quantitatively assessed using a rotating disk electrode (RDE) in O_2-saturated 0.1 M KOH electrolyte, with polarization curves acquired at 1600 rpm under a standard three-electrode configuration. As depicted in Figure 3a, $FeMn_{DSA}$/*d*NC demonstrates superior ORR performance, achieving a half-wave potential ($E_{1/2}$) of 0.921 V (vs. RHE), which is 27 mV, 39 mV, and 46 mV higher than that of $FeMn_{DSA}$/NC, Fe_{SA}/NC, and 20 wt% Pt/C, respectively. This remarkable activity is attributed to the defect-engineered FeMn diatomic architecture, which optimizes d-band electron distribution to promote ORR. To prove the MA-induced defect effects, we systematically evaluated the ORR performance of $FeMn_{DSA}$/*d*NC catalysts under varied MA loadings (200-600 mg). As evidenced in Figure S19, $FeMn_{DSA}$/*d*NC-400 mg delivers peak activity due to an optimal balance between defect density and structural stability.

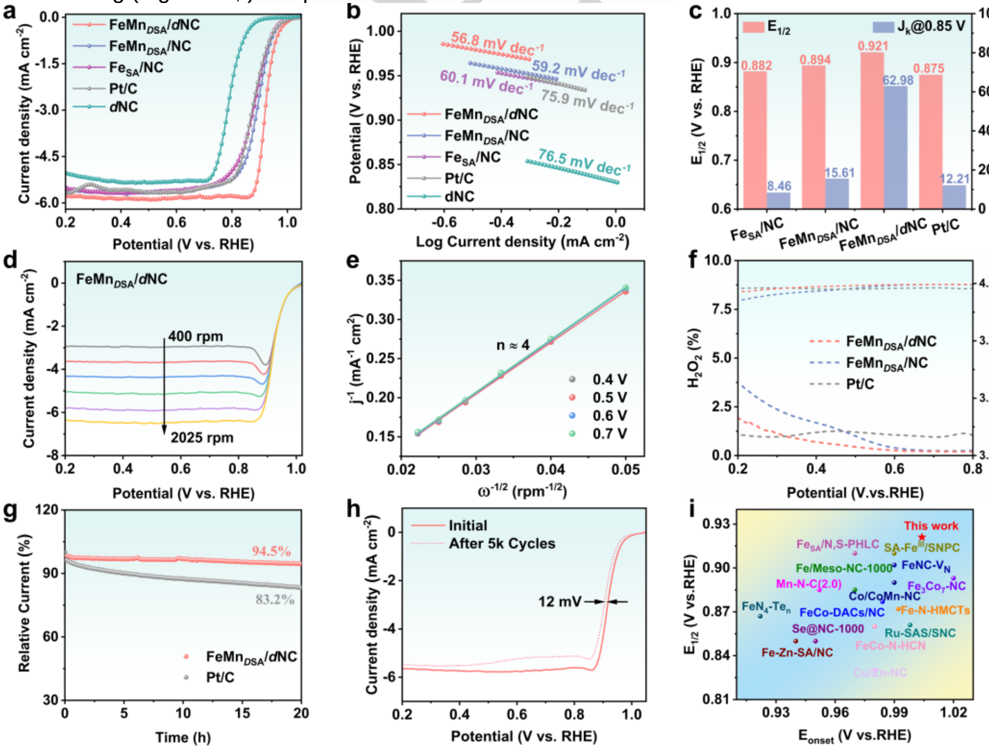

Figure 3. Electrochemical ORR performance. (a) LSV curves recorded for $FeMn_{DSA}$/*d*NC and reference samples at 1600 rpm in O_2-saturated 0.1 M KOH. (b) Tafel plots. (c) Comparison of J_k at 0.85 V and $E_{1/2}$. (d, e) LSV curves of $FeMn_{DSA}$/*d*NC at varied rotating speeds and calculated K-L plots. (f) Electron-transfer number and H_2O_2 yield of $FeMn_{DSA}$/*d*NC. (g) Chronoamperometric responses of $FeMn_{DSA}$/*d*NC and Pt/C. (h) LSV curves of $FeMn_{DSA}$/*d*NC before and after 5000 CV cycles. (i) Comparison of E_{onset} and $E_{1/2}$ values for $FeMn_{DSA}$/*d*NC and previously reported ORR catalysts.

Kinetic superiority is further evidenced by the Tafel slope of $FeMn_{DSA}/dNC$ (56.8 mV/dec, Figure 3b), which is lower than that of $FeMn_{DSA}/NC$ (59.2 mV/dec), Fe_{SA}/NC (60.1 mV/dec), and Pt/C (75.9 mV/dec). Additionally, the kinetic current density (J_k) of $FeMn_{DSA}/dNC$ at 0.85 V vs. RHE reaches 62.98 mA cm^{-2}, exceeding all counterparts (Figure 3c). Electrochemical impedance spectroscopy (EIS) confirms its minimal charge transfer resistance (Figure S20), indicative of rapid interfacial electron dynamics of $FeMn_{DSA}/dNC$.[18] Rotating speed-dependent linear sweep voltammetry (LSV) and derived Koutecky-Levich (K-L) plots (Figure 3d,e and S21) exhibit linearity within the potential range of 0.4-0.7 V (vs. RHE), resulting in an electron transfer number (n) of ~4.0 for $FeMn_{DSA}/dNC$. Rotating ring-disk electrode (RRDE) analyses (Figure 3f) corroborate a dominant four-electron pathway, with H_2O_2 yield below 2.5% and $n \approx 4.0$ across 0.2-0.8 V vs. RHE. The stability of $FeMn_{DSA}/dNC$ was assessed through chronoamperometric testing. As depicted in Figure 3g, it maintains 94.5% initial current after 20 h of continuous operation in 0.1 M KOH, while the Pt/C catalyst remains only 83.2%. After 5000 cyclic voltammetry (CV) cycles between 0.6 V and 1.0 V vs. RHE (Figure 3h), the $E_{1/2}$ of $FeMn_{DSA}/dNC$ decreased by just 12 mV, both confirming its excellent long-term stability. Notably, the $FeMn_{DSA}/dNC$ catalyst surpasses other non-precious metal-based electrocatalysts documented in the literature (Figure 3i and Table S3), positioning it at the forefront of advanced electrocatalyst design.

In-situ attenuated total reflectance surface-enhanced infrared absorption spectroscopy (ATR-SEIRAS) was conducted to identify critical oxygen reduction intermediates on $FeMn_{DSA}/dNC$. Progressive potential polarization from open-circuit voltage to 0.1 V vs. RHE intensifies interfacial water bending (1643 cm^{-1}) and O–H stretching (3370 cm^{-1}) modes (Figure 5a), signifying hydroxyl group accumulation during ORR.[19] Meanwhile, the distinct vibrational bands at 1170 cm^{-1} ($^*OOH$) and 1068 cm^{-1} ($^*O^{2-}$), confirm mono-site adsorption of $^*OOH$ intermediates[20], highlighting the well-defined adsorption characteristics of the active sites. Density functional theory (DFT) calculations were performed to elucidate the ORR mechanism of $FeMn_{DSA}/dNC$ and assess the impact of defects on the local coordination environment and electronic structure at the atomic level. Three configuration models, Fe_{SA}/NC, $FeMn_{DSA}/NC$, and $FeMn_{DSA}/dNC$, were constructed for comparative analysis (Figure S22). Gibbs free energy (ΔG) profiles (Figures S23,S24) for each ORR step indicate a spontaneous exothermic reaction at U = 0 V. At the equilibrium potential (U = 1.23 V), the rate-determining step (RDS) for $^*OH$ desorption in Fe_{SA}/NC has an energy barrier of 0.83 V. In contrast, for $FeMn_{DSA}/NC$ and $FeMn_{DSA}/dNC$, the RDS shifts to $^*OOH$ formation, with energy barriers of 0.72 V and 0.40 V, respectively (Figure 4b). Density of states (DOS) analysis was employed to investigate the electronic structural modifications of DSAs mediated by defects. The d-band center of the Fe site in $FeMn_{DSA}/dNC$ shifts from -1.52 eV to -1.38 eV relative to $FeMn_{DSA}/NC$, indicating a decrease in antibonding orbital

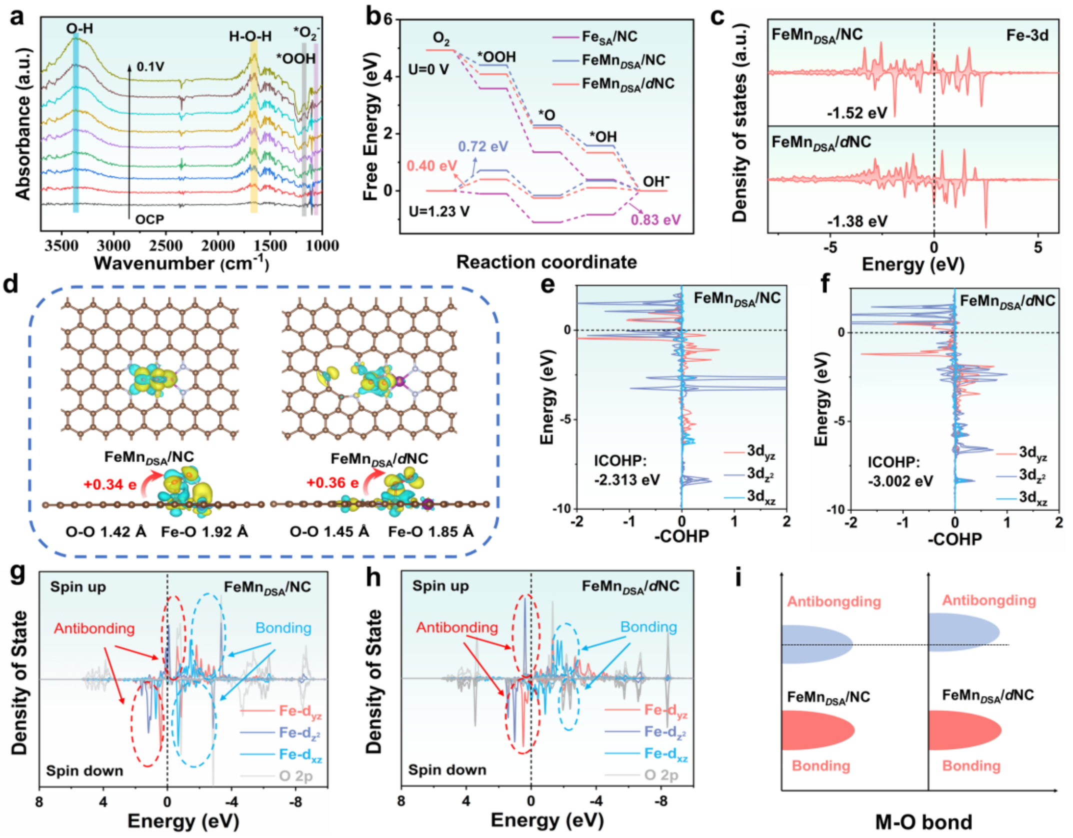

Figure 4. In-situ ATR-SEIRAS and theoretical analysis. (a) Potential-dependent in-situ ATR-SEIRAS spectra for $FeMn_{DSA}/dNC$, with the potential interval of 100 mV. (b) Free energy diagrams for the corresponding three samples. (c) DOS of Fe site for $FeMn_{DSA}/NC$ and $FeMn_{DSA}/dNC$. (d) Charge density difference and Bader charge analysis of $^*OOH$ adsorbed on $FeMn_{DSA}/NC$ and $FeMn_{DSA}/dNC$. (e,f) pCOHP of $^*OOH$ adsorbed, (g,h) PDOS of Fe 3d and O 2p orbital for $FeMn_{DSA}/NC$ and $FeMn_{DSA}/dNC$. (i) Schematic illustration of Fe-$^*OOH$ bond formation for $FeMn_{DSA}/NC$ and $FeMn_{DSA}/dNC$.

occupation and a more robust interaction with O_2 (Figure 4c). Charge difference density and Bader charge analyses (Figure 4d) reveal that defect engineering amplifies electron donation from Fe active sites in $FeMn_{DSA}/d$NC to adsorbed *OOH intermediates (0.36 e^- vs. 0.34 e^- in $FeMn_{DSA}$/NC), reinforcing stronger Fe-O interactions. Correspondingly, *OOH adsorption on $FeMn_{DSA}/d$NC features an elongated O-O bond (1.45 Å vs. 1.42 Å) and a shortened Fe-O bond (1.85 Å vs. 1.92 Å) compared to $FeMn_{DSA}$/NC, collectively strengthening *OOH activation kinetics. Further analysis through crystal orbital hamiltonian population (COHP) analysis reveals that the Fe-O bond strength in $FeMn_{DSA}/d$NC (-3.002 eV) is stronger than that in $FeMn_{DSA}$/NC (-2.313 eV) upon *OOH adsorption. This enhancement is primarily attributed to the hybridization of Fe $3d_{z^2}$ orbitals with O 2p orbitals, accompanied by additional contributions from the d_{yz} and d_{xz} orbitals (Figure 4e,f and Tables S5–S7). Projected DOS (PDOS) analysis of Fe 3d and O 2p orbitals after *OOH adsorption (Figure 4g-i) reveals a larger energy gap between bonding and antibonding states in the spin-up configuration of $FeMn_{DSA}/d$NC compared to $FeMn_{DSA}$/NC, which enhances Fe-O bonding and corroborates Bader charge analysis. DFT calculation results demonstrate that the synergistic interplay between heteronuclear DSA coordination and defect-driven electronic restructuring reduces the ORR activation energy barrier, approaching the Sabatier volcano plot apex.

The practical efficacy of $FeMn_{DSA}/d$NC was validated in zinc-air batteries (ZABs) employing it or Pt/C as air cathodes (Figure 5a). The $FeMn_{DSA}/d$NC-based ZAB achieves a superior open-circuit voltage of 1.50 V, surpassing that of the Pt/C-based ZAB (1.48 V) (Figure 5b). Additionally, it delivers a peak power density of 291 mW cm^{-2} at a current density of 557 mA cm^{-2}, higher than the Pt/C-based ZAB (217 mW cm^{-2} at 419 mA cm^{-2}) (Figure 5c). The stepped discharge curves (Figure 5d) illustrate that the $FeMn_{DSA}/d$NC-based ZAB sustains a stable discharge plateau even at elevated current densities. When the current density is reduced back to 2 mA cm^{-2}, the plateau remains virtually unaffected, underscoring its remarkable reversibility and stability. At a constant 10 mA cm^{-2}, the $FeMn_{DSA}/d$NC-based ZAB demonstrates a specific capacity of 817 mA h g^{-1}, outperforming the Pt/C-based ZAB (665 mA h g^{-1}) (Figure 5e). Furthermore, a single $FeMn_{DSA}/d$NC-based ZAB powers a blue light-emitting diode (LED), showcasing its practical viability (Figure 5b inset). To evaluate the cycling performance, a ZAB with the $FeMn_{DSA}/d$NC+RuO_2 cathode was tested through to charge-discharge cycling at 5mA cm^{-2}. Impressively, the $FeMn_{DSA}/d$NC+RuO_2-based ZAB maintains a stable voltage

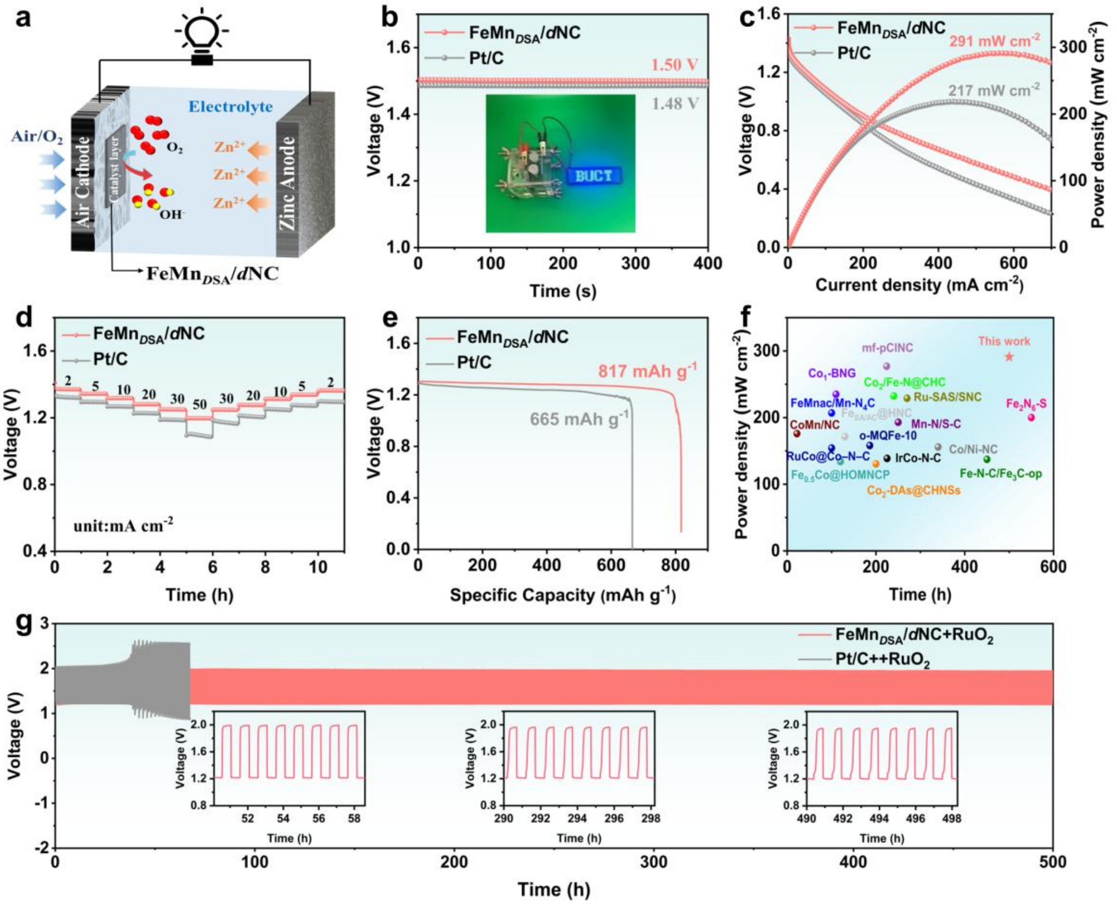

Figure 5. Zinc-air (ZAB) battery performance of $FeMn_{DSA}/d$NC-based ZAB and comparison with Pt/C-based ZAB. (a) Schematic illustration of ZAB. (b) Open circuit potential, with an inset photograph of an LED lamp powered by $FeMn_{DSA}/d$NC-based ZAB. (c) Polarization curves and corresponding power densities. (d) Galvanostatic discharge curves at various current densities. (e) Specific capacity evaluation at 10 mA cm^{-2}. (f) Peak power density and runtime of rechargeable $FeMn_{DSA}/d$NC-based ZAB compared to previously reported ZABs. (g) Galvanostatic discharge-charge cycle profiles of ZAB based on $FeMn_{DSA}/d$NC+RuO_2 and Pt/C+RuO_2 at 5 mA cm^{-2}.

gap of 0.79 V over 500 h of prolonged functioning with negligible voltage decay (Figure 5g), whereas the Pt/C+RuO$_2$-based ZAB degrades rapidly within 50 h. The FeMn$_{DSA}$/*d*NC-based ZAB rivals the majority of state-of-the-art ZABs reported in recent literature (Figure 5f and Table S4), accentuating its potential as a high-performance and durable alternative to Pt-based systems.

Conclusion

In summary, we have achieved atomic-precision immobilization of heteronuclear Fe-Mn diatomic pairs within defect-rich nitrogen-doped carbon matrices through the precisely engineered TDT synthetic protocal, where orchestrated defect traps simultaneously stabilize metal sites and tailor d-orbital hybridization. The synergistic electronic effects endow FeMn$_{DSA}$/*d*NC with exceptional ORR electrocatalysis in alkaline media, exhibiting a high half-wave potential of 0.921 V, 46 mV superior to benchmark Pt/C. When integrated into zinc-air batteries, it achieves a peak power density of 291 mW cm^{-2} and sustains stable charge-discharge cycling for 500 h. In-situ spectroscopy and DFT calculations reveal that defect-mediated FeMn interactions enhance electron transfer from Fe sites to *OOH intermediates, reinforcing Fe 3d_{z^2}-O 2p hybridization, which consequently alters the RDS and reduces the ORR activation energy barrier, bringing it closer to the Sabatier volcano peak. This work presents a novel strategy for the targeted synthesis of DSAs and elucidates the mechanisms of their intrinsic activity, driving the development of advanced electrocatalysts for energy storage and conversion.

Acknowledgements

Thanks for the support by the Strategic Priority Research Program of the Chinese Academy of Sciences, Grant No. XDB0600000, XDB0600100, National Natural Science Foundation of China, Grant No. 22302205, National Natural Science Foundation of China, Grant No. 22372006, Open Research Fund of Suzhou Laboratory, Grant No. SZLAB-1308-2024-ZD009 and State Key Laboratory of Catalysis, No 2024SKL-B-008.

Keywords: heteronuclear diatomic sites • defect engineering • d-band center modulation • oxygen reduction reaction • Zn-air battery

[1] a) S. Z. Oener, M. J. Foster, S. W. Boettcher, *Science* **2020**, *369*, 1099-1103; b) D. A. Cullen, K. C. Neyerlin, R. K. Ahluwalia, R. Mukundan, K. L. More, R. L. Borup, A. Z. Weber, D. J. Myers, A. Kusoglu, *Nat. Energy* **2021**, *6*, 462-474; c) H. N. Nong, L. J. Falling, A. Bergmann, M. Klingenhof, H. P. Tran, C. Spöri, R. Mom, J. Timoshenko, G. Zichittella, A. Knop-Gericke, S. Piccinin, J. Pérez-Ramírez, B. R. Cuenya, R. Schlögl, P. Strasser, D. Teschner, T. E. Jones, *Nature* **2020**, *587*, 408-413.

[2] a) X. Xie, C. He, B. Li, Y. He, D. A. Cullen, E. C. Wegener, A. J. Kropf, U. Martinez, Y. Cheng, M. H. Engelhard, M. E. Bowden, M. Song, T. Lemmon, X. S. Li, Z. Nie, J. Liu, D. J. Myers, P. Zelenay, G. Wang, G. Wu, V. Ramani, Y. Shao, *Nat. Catal.* **2020**, *3*, 1044-1054; b) M. Liu, J. Zhang, H. Su, Y. Jiang, W. Zhou, C. Yang, S. Bo, J. Pan, Q. Liu, *Nat. Commun.* **2024**, *15*, 1675; c) Y. Zhao, Z. Zhang, L. Liu, Y. Wang, T. Wu, W. Qin, S. Liu, B. Jia, H. Wu, D. Zhang, X. Qu, G. Qi, E. P. Giannelis, M. Qin, S. Guo, *J. Am. Chem. Soc.* **2022**, *144*, 20571-20581.

[3] a) K. Kodama, T. Nagai, A. Kuwaki, R. Jinnouchi, Y. Morimoto, *Nat. Nanotechnol.* **2021**, *16*, 140-147; b) D. Frattini, E. García Gaitán, A. Bustinza Murguialday, M. Armand, N. Ortiz-Vitoriano, *Energy Environ. Sci.* **2022**, *15*, 5039-5058; c) F. Xiao, Q. Wang, G.-L. Xu, X. Qin, I. Hwang, C.-J. Sun, M. Liu, W. Hua, H.-w. Wu, S. Zhu, J.-C. Li, J.-G. Wang, Y. Zhu, D. Wu, Z. Wei, M. Gu, K. Amine, M. Shao, *Nat. Catal.* **2022**, *5*, 503-512.

[4] a) X. Guo, G. Fang, G. Li, H. Ma, H. Fan, L. Yu, C. Ma, X. Wu, D. Deng, M. Wei, D. Tan, R. Si, S. Zhang, J. Li, L. Sun, Z. Tang, X. Pan, X. Bao, *Science* **2014**, *344*, 616-619; b) J. Li, W. Xia, X. Xu, D. Jiang, Z.-X. Cai, J. Tang, Y. Guo, X. Huang, T. Wang, J. He, B. Han, Y. Yamauchi, *J. Am. Chem. Soc.* **2023**, *145*, 27262-27272; c) X. Ren, J. Zhao, X. Li, J. Shao, B. Pan, A. Salamé, E. Boutin, T. Groizard, S. Wang, J. Ding, X. Zhang, W.-Y. Huang, W.-J. Zeng, C. Liu, Y. Li, S.-F. Hung, Y. Huang, M. Robert, B. Liu, *Nat. Commun.* **2023**, *14*, 3401; d) S. Wang, L. Wang, D. Wang, Y. Li, *Energy Environ. Sci.* **2023**, *16*, 2759-2803.

[5] a) M. Yuan, Y. Liu, Y. Du, Z. Xiao, H. Li, K. Liu, L. Wang, *Adv. Funct. Mater.* **2024**, *34*, 2401484; b) L.-J. Yuan, B. Liu, L.-x. Shen, Y.-K. Dai, Q. Li, C. Liu, W. Gong, X.-L. Sui, Z.-B. Wang, *Adv. Mater.* **2023**, *35*, 2305945; c) Y. Li, H. Sun, L. Ren, K. Sun, L. Gao, X. Jin, Q. Xu, W. Liu, X. Sun, *Angew. Chem., Int, Ed,* **2024**, *63*, e202405334.

[6] a) T. He, Y. Chen, Q. Liu, B. Lu, X. Song, H. Liu, M. Liu, Y.-N. Liu, Y. Zhang, X. Ouyang, S. Chen, *Angew. Chem., Int, Ed,* **2022**, *61*, e202201007; b) J. Qiao, Y. You, L. Kong, W. Feng, H. Zhang, H. Huang, C. Li, W. He, Z. Sun, *Adv. Mater.* **2024**, *36*, 2405533; c) C. Hu, G. Xing, W. Han, Y. Hao, C. Zhang, Y. Zhang, C.-H. Kuo, H.-Y. Chen, F. Hu, L. Li, S. Peng, *Adv. Mater.* **2024**, *36*, 2405763.

[7] Z. Jiang, X. Liu, X.-Z. Liu, S. Huang, Y. Liu, Z.-C. Yao, Y. Zhang, Q.-H. Zhang, L. Gu, L.-R. Zheng, L. Li, J. Zhang, Y. Fan, T. Tang, Z. Zhuang, J.-S. Hu, *Nat. Commun.* **2023**, *14*, 1822.

[8] Y. Wang, J. Wu, S. Tang, J. Yang, C. Ye, J. Chen, Y. Lei, D. Wang, *Angew. Chem., Int, Ed,* **2023**, *62*, e202219191.

[9] a) X. Wang, Y. Jia, X. Mao, D. Liu, W. He, J. Li, J. Liu, X. Yan, J. Chen, L. Song, A. Du, X. Yao, *Adv. Mater.* **2020**, *32*, 2000966; b) S. Ji, Y. Wang, H. Liu, X. Lu, C. Guo, S. Xin, J. H. Horton, F. Zhan, Y. Wang, Z. Li, *Adv. Funct. Mater.* **2024**, *34*, 2314621; c) H. Tian, A. Song, P. Zhang, K. Sun, J. Wang, B. Sun, Q. Fan, G. Shao, C. Chen, H. Liu, Y. Li, G. Wang, *Adv. Mater.* **2023**, *35*, 2210714.

[10] Y. Zhao, H.-C. Chen, X. Ma, J. Li, Q. Yuan, P. Zhang, M. Wang, J. Li, M. Li, S. Wang, H. Guo, R. Hu, K.-H. Tu, W. Zhu, X. Li, X. Yang, Y. Pan, *Adv. Mater.* **2024**, *36*, 2308243.

[11] Y.-S. Wei, L. Sun, M. Wang, J. Hong, L. Zou, H. Liu, Y. Wang, M. Zhang, Z. Liu, Y. Li, S. Horike, K. Suenaga, Q. Xu, *Angew. Chem., Int, Ed,* **2020**, *59*, 16013-16022.

[12] a) M. Tavakkoli, E. Flahaut, P. Peljo, J. Sainio, F. Davodi, E. V. Lobiak, K. Mustonen, E. I. Kauppinen, *ACS Catal.* **2020**, *10*, 4647-4658; b) W. Yao, A. Hu, J. Ding, N. Wang, Z. Qin, X. Yang, K. Shen, L. Chen, Y. Li, *Adv. Mater.* **2023**, *35*, 2301894; c) Y. He, X. Yang, Y. Li, L. Liu, S. Guo, C. Shu, F. Liu, Y. Liu, Q. Tan, G. Wu, *ACS Catal.* **2022**, *12*, 1216-1227.

[13] L. Lyu, X. Hu, S. Lee, W. Fan, G. Kim, J. Zhang, Z. Zhou, Y.-M. Kang, *J. Am. Chem. Soc.* **2024**, *146*, 4803-4813.

[14] a) T. Cui, Y.-P. Wang, T. Ye, J. Wu, Z. Chen, J. Li, Y. Lei, D. Wang, Y. Li, *Angew. Chem., Int, Ed,* **2022**, *61*, e202115219; b) X. Xu, T. Tang, G. Zhang, J. Guan, *Nano Energy* **2024**, *131*, 110294.

[15] a) H. Liu, L. Jiang, J. Khan, X. Wang, J. Xiao, H. Zhang, H. Xie, L. Li, S. Wang, L. Han, *Angew. Chem., Int, Ed,* **2023**, *62*, e202214988; b) X. Bai,

Y. Wang, J. Han, S. Chen, X. Niu, J. Guan, *Chem. Sci.,* **2024**, *15*, 19466-19472; c) X. Bai, J. Han, S. Chen, X. Niu, J. Guan, *Chin. J. Catal.* **2023**, *54*, 212-219.

[16] D. Cao, Y. Mu, L. Liu, Z. Mou, S. Chen, W. Yan, H. Zhou, T.-S. Chan, L.-Y. Chang, L. Song, H.-J. Zhai, X. Fan, *ACS Nano* **2024**, *18*, 11474-11486.

[17] a) S. Huang, Z. Qiao, P. Sun, K. Qiao, K. Pei, L. Yang, H. Xu, S. Wang, Y. Huang, Y. Yan, D. Cao, *Appl. Catal. B.* **2022**, *317*, 121770; b) X. Xie, L. Shang, X. Xiong, R. Shi, T. Zhang, *Adv. Enery Mater.* **2022**, *12*, 2102688; c) Y. Zhu, Y. Jiang, H. Li, D. Zhang, L. Tao, X.-Z. Fu, M. Liu, S. Wang, *Angew. Chem., Int, Ed,* **2024**, *63*, e202319370.

[18] a) V. Vivier, M. E. Orazem, *Chem. Rev.* **2022**, *122*, 11131-11168; b) S. Wang, J. Zhang, O. Gharbi, V. Vivier, M. Gao, M. E. Orazem, *Nat. Rev. Methods Primers* **2021**, *1*, 41; c) X. Wang, N. Zhang, S. Guo, H. Shang, X. Luo, Z. Sun, Z. Wei, Y. Lei, L. Zhang, D. Wang, Y. Zhao, F. Zhang, L. Zhang, X. Xiang, W. Chen, B. Zhang, *J. Am. Chem. Soc.* **2024**, *146*, 21357-21366.

[19] J. Hu, W. Shang, C. Xin, J. Guo, X. Cheng, S. Zhang, S. Song, W. Liu, F. Ju, J. J. A. C. Hou, *Angew. Chem., Int, Ed,* **2023**, *135*, e202304754.

[20] W. Zhou, B. Li, X. Liu, J. Jiang, S. Bo, C. Yang, Q. An, Y. Zhang, M. A. Soldatov, H. Wang, S. Wei, Q. Liu, *Nat. Commun.* **2024**, *15*, 6650.

Entry for the Table of Contents

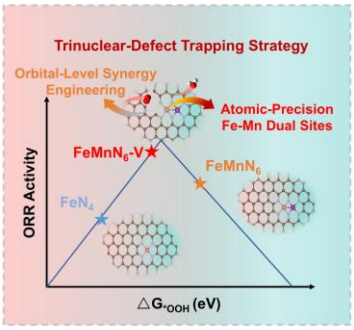

A defect-engineered heteronuclear FeMn dual-atom catalyst on a porous N-doped carbon matrix is synthesized via a customized trinuclear-defect trapping strategy. The defect-mediated coordination strengthens Fe 3$d_z{}^2$ with O 2p orbital hybridization, optimizing adsorption energy toward Sabatier optimality. The catalyst delivers a 0.921 V half-wave potential for alkaline oxygen reduction and excellent Zn-air battery performance.